# Isospin transport phenomena for the systems $^{80}$Kr + $^{40,48}$Ca at 35 MeV/nucleon

S. Piantelli,[1,*] G. Casini,[1] A. Ono,[2] G. Poggi,[1,3] G. Pastore,[1,3] S. Barlini,[1,3] M. Bini,[1,3] A. Boiano,[4] E. Bonnet,[5] B. Borderie,[6] R. Bougault,[7] M. Bruno,[8,9,†] A. Buccola,[1,3] A. Camaiani,[1,3] A. Chbihi,[10] C. Ciampi,[1,3] M. Cicerchia,[11] M. Cinausero,[11] M. Degerlier,[12] J. A. Dueñas,[13] Q. Fable,[10] D. Fabris,[14] J. D. Frankland,[10] C. Frosin,[1,3] F. Gramegna,[11] D. Gruyer,[7] A. Kordyasz,[15] T. Kozik,[16] J. Lemarié,[10] N. Le Neindre,[7] I. Lombardo,[17] O. Lopez,[7] G. Mantovani,[11,18,19] T. Marchi,[11] M. Henri,[10] L. Morelli,[8,9] A. Olmi,[1] P. Ottanelli,[1,3] M. Pârlog,[7,20] G. Pasquali,[1,3] J. Quicray,[7] A. A. Stefanini,[1,3] G. Tortone,[4] S. Upadhyaya,[16] S. Valdré,[1] G. Verde,[17] E. Vient,[7] and M. Vigilante[4,21]
(FAZIA Collaboration)

[1]*INFN Sezione di Firenze, I-50019 Sesto Fiorentino, Italy*
[2]*Department of Physics, Tohoku University, Sendai 980-8578, Japan*
[3]*Dipartimento di Fisica, Università di Firenze, I-50019 Sesto Fiorentino, Italy*
[4]*INFN Sezione di Napoli, 80126 Napoli, Italy*
[5]*SUBATECH, Université de Nantes, IMT Atlantique, IN2P3/CNRS, 44307 Nantes Cedex 3, France*
[6]*Université Paris-Saclay, CNRS/IN2P3, IJCLab, 91405 Orsay, France*
[7]*Normandie Univ, ENSICAEN, UNICAEN, CNRS/IN2P3, LPC Caen F-14000 Caen, France*
[8]*Dipartimento di Fisica, Università di Bologna, 40127 Bologna, Italy*
[9]*INFN Sezione di Bologna, 40127 Bologna, Italy*
[10]*GANIL, CEA/DRF-CNRS/IN2P3, 14076 Caen, France*
[11]*INFN Laboratori Nazionali di Legnaro, 35020 Legnaro, Italy*
[12]*Physics Department of Nevsehir Haci Bektas Veli University, Nevsehir (Turkey)*
[13]*Departamento de Ingeniería Eléctrica y Centro de Estudios Avanzados en Física, Matemáticas y Computación, Universidad de Huelva, 21007 Huelva, Spain*
[14]*INFN Sezione di Padova, 35131 Padova, Italy*
[15]*Heavy Ion Laboratory, University of Warsaw, 02-093 Warszawa, Poland*
[16]*Faculty of Physics, Astronomy and Applied Computer Science, Jagiellonian University, 30-348 Cracow, Poland*
[17]*INFN Sezione di Catania, 95123 Catania, Italy*
[18]*Dipartimento di Fisica, Università di Padova, 35131 Padova, Italy*
[19]*Universidade de Santiago de Compostela, Santiago de Compostela, Spain*
[20]*"Horia Hulubei" National Institute for R&D in Physics and Nuclear Engineering (IFIN-HH), P. O. Box MG-6, Bucharest Magurele, Romania*
[21]*Dipartimento di Fisica, Università di Napoli, 80126 Napoli, Italy*

(Received 4 May 2020; accepted 12 November 2020; published 8 January 2021)

Experimental data concerning isospin transport phenomena for the systems $^{80}$Kr + $^{40,48}$Ca at 35 MeV/nucleon are presented. Data have been collected with four FAZIA blocks; this data set is the same analyzed in S. Piantelli *et al.*, Phys. Rev. C **101**, 034613 (2020). The isotopic composition of the QuasiProjectile residue (up to $Z$ around 25) and of its decay products in the two reactions are compared, finding a neutron enrichment when the target is $^{48}$Ca. The isotopic composition of the emitted light charged particles (LCP) and intermediate mass fragments (IMF) was also investigated in different windows of velocity. The obtained results have been compared with the prediction of the transport model AMD followed by the statistical code GEMINI (used as an afterburner), with different recipes for the density dependence of the symmetry energy term in the nuclear equation of state. A weak indication in favor of a stiff symmetry energy emerges when the fragments emitted at midvelocity are examined.

DOI: 10.1103/PhysRevC.103.014603

## I. INTRODUCTION

In the literature many experimental evidences about the so-called isospin transport phenomena in heavy-ion collisions around Fermi energies (20–50 MeV/nucleon) can be found, e.g., Refs. [1–14]. The term "isospin transport" indicates all the cases in which the isotopic composition of the ejectiles depends on the velocity region they belong to and cases in which the isotopic composition of the ejectiles associated to the phase space of one of the reaction partners depends on the isotopic composition of the other one. The amount of isospin transport is related to the symmetry energy term of the

*Corresponding author: piantelli@fi.infn.it
†Deceased.

 

nuclear equation of state for isospin-asymmetric matter. The dependence of the isotopic composition of the ejectiles on the velocity can be easily put into evidence in symmetric reactions. Comparing reactions with targets of different isotopic composition, being equal in the beam energy and the projectile, it is instead possible to evidence the effect of changing the isotopic composition of one reaction partner on the isotopic contents of the ejectiles associated to the other one.

In particular, in peripheral and semiperipheral reactions, where the cross section is dominated by binary collisions, with two outcoming heavy fragments, the quasiprojectile (QP) and the quasitarget (QT), at the end of the interaction phase, the isospin of the QP depends on the $N/Z$ of the target. Clear examples of this effect, although at a slightly lower beam energy with respect to the Fermi energy domain, can be found in Refs. [10] and [13]. In Ref. [10] a $^{86}$Kr beam at 15 MeV/nucleon and two Sn targets, a neutron-rich $^{124}$Sn and a neutron-poor $^{112}$Sn, were used; the isotopic composition of the QP was measured by means of the momentum achromat recoil spectrometer (MARS) [15], finding a shift toward the neutron-rich side when the target is the neutron-rich one and vice versa. In Ref. [13] the $\langle N\rangle/Z$ vs. $Z$ of the QP, coming from a $^{32}$S beam at 17.7 MeV/nucleon, was found to be systematically higher when the target was the neutron-rich $^{48}$Ca compared with the case of $^{40}$Ca. Also the isotopic composition of the QP decay products depends on the neutron richness of the target, as shown, for example, in Ref. [9], where the isotopic composition of complex particles emitted from the QP is more neutron rich in the reaction on $^{197}$Au than in the reaction on $^{58}$Ni, for a beam of $^{58}$Ni at 52 and 74 MeV/nucleon. Similarly in Ref. [13] the $d/p$ and $t/p$ ratios for particles forward emitted with respect to the QP were found to depend on the neutron richness of the target, although the projectile was the same. In Ref. [12], where only inclusive data were available because only one prototype FAZIA telescope, placed at forward angles, was used, the $\langle N\rangle/Z$ vs. $Z$ of the ejectiles was systematically higher when the target was the neutron-rich $^{124}$Sn compared with that obtained when the target was $^{112}$Sn. In Ref. [7] the isobaric yield ratio $^{7}$Li / $^{7}$Be for fragments emitted from the QP shows a dependence on the neutron richness of the target: For a given beam of $^{40}$Ca at 25 MeV/nucleon the ratio is higher when the target is $^{48}$Ca with respect to the case with the $^{40}$Ca target. In Ref. [8] the isobaric ratios of light products emitted by the QP is compared for systems with Ca beams at 32 MeV/nucleon and Sn targets with different isotopic composition; it was found that the $N/Z$ value of the QP (reconstructed by means of a fitting procedure and normalized to that of the total system) depends on the isotopic composition of the target and it is intermediate between that of the projectile and that of the total system, thus corresponding to an incomplete isospin equilibration between target and projectile.

In peripheral and semiperipheral reactions around the Fermi energy a considerable amount of light charged particles (LCP) and mainly intermediate mass fragments (IMF) are emitted at midvelocity, i.e., at velocities intermediate between that of QP and QT; this emission, which takes place on shorter timescales with respect to the statistical deexcitation of QP and QT, might originate from the rupture of a "neck" of nuclear matter formed during the interaction phase. If the isotopic composition of midvelocity LCP and IMF is compared with that of the ejectiles coming from the statistical deexcitation of QP and QT, a neutron enrichment is observed for the former emission. Examples of such effects can be found for example in Ref. [11], where the $\langle N\rangle/Z$ of midvelocity IMF is shown to be systematically higher than that of IMF evaporated by QP or QT. Within the limits of an inclusive measurement, in Ref. [12] the $\langle N\rangle/Z$ of light IMF with velocity closer to the center-of-mass (c.m.) value is considerably higher than that of the IMF with the same $Z$ emitted with velocity closer to the QP. In Ref. [7] the isobaric yield ratio $^{7}$Li / $^{7}$Be is higher for fragments emitted at midvelocity than for fragments emitted from the QP. In Ref. [4] the authors simultaneously measured neutrons and charged particles in the symmetric reaction $^{64}$Zn + $^{64}$Zn at 45 MeV/nucleon; they separated the contribution of the QP source from that of the midvelocity source using a moving source fit, and they found that the $N/Z$ at midvelocity (including all the detected products, free neutrons included) is considerably higher than that at the velocity of the QP. Other examples of neutron enrichment for the midvelocity emission can be found in Ref. [1] or Ref. [2] and in Ref. [16].

When a proper combination of neutron-rich and neutron-deficient systems is available, in order to investigate the isospin transport process the isospin transport ratio introduced in Ref. [17] can be used, as shown, e.g., in Refs. [3,6,14]; this technique is extremely powerful because it allows to minimize undesired effects introducing linear perturbations with respect to the primary fragment partitions [18], such as pre-equilibrium emission or sequential decay.

From the theoretical point of view, the isospin transport mechanism is generally attributed to the fact that neutrons and protons are subject to different forces; two contributions can be put into evidence, a diffusion process, driven by the isospin-asymmetry gradient between target and projectile, and a drift one, driven by the density gradient between different regions of the interacting system [19]. The latter can favor a neutron enrichment at midvelocity with respect to the QP/QT regions in peripheral and semiperipheral collisions, because the midvelocity zone is supposed to be at density $\rho$ lower than the saturation value $\rho_0$ typical of the evaporating QP/QT. However, it must be considered that the fractionation mechanism (i.e., the fact that in dilute isospin-asymmetric nuclear matter the gas phase is more neutron rich than the liquid one [20–22]) may reduce the isospin content of the midvelocity fragments. Since the amount of isospin transport is related to the symmetry energy term of the nuclear equation of state for isospin-asymmetric matter, some hints about such a term can be drawn by comparing the experimental results on observables related to the isospin transport process with the prediction of transport models, able to give a good general description of the reaction phenomenology, with different hypotheses for the density dependence of the symmetry energy term. Of course, this method works provided that the system explores regions sufficiently far from $\rho_0$; in fact close to $\rho_0$ (more precisely at $\sim\frac{2}{3}\rho_0$, corresponding to the average density of atomic nuclei) all symmetry energy predictions are constrained by the value given by the semiempirical mass formula

but not the slope parameter $L$[1], which is less well constrained [24]. For example, in Ref. [11] the authors found a better reproduction of the $\langle N\rangle/Z$ vs. $Z$ of the midvelocity emitted IMF for the system $^{124}$Sn + $^{64}$Ni at 35 MeV/nucleon with an asystiff ($L = 80$ MeV) parametrization of the symmetry energy; they used SMF [25] (followed by GEMINI [26,27] as an afterburner) as transport model to compare with the experimental data. No sensitivity to the symmetry energy density dependence was found in Ref. [13] at lower beam energy (17.7 MeV/nucleon) looking at the $\langle N\rangle/Z$ vs. $Z$ of the QP; in this case the adopted model was again SMF followed by GEMINI++ [28]. This time the lack of sensitivity was expected, because below 20 MeV/nucleon the system is supposed to stay close to normal density. However, even at higher beam energies (52 and 74 MeV/nucleon) in Ref. [29], comparing the experimental data with SMF followed by SIMON [30] as an afterbuner, the authors found that neither the $\langle N\rangle/Z$ vs. $Z$ of the QP nor that of the complex particles emitted by the QP show a significant dependence on the symmetry energy parametrization; also this finding is justified as due to the small range in density around $\rho_0$ experienced by the QP during the reaction. From these observations it seems that the isotopic composition of the QP and of its decay products are not the most suitable tool to investigate the symmetry energy term, though they may still be useful observables to test the symmetry energy when they are analyzed in the form of the isospin transport ratio. Clearer constraints might be obtained looking at the isotopic composition of midvelocity products, because in that case a wider range in $\rho$ (on the low density side with respect to $\rho_0$) is tested. However, the most promising tool to test the symmetry energy seems to be the isospin transport ratio [31], although the fact that it is necessary to rely on models not always agreeing among themselves may represent a real limitation of the technique. For example, in Ref. [3] the experimental results were compared with those of a BUU code [32], finding indication of a rather stiff symmetry energy. At variance, in Ref. [33] and Ref. [34], which both used ImQMD [35] as reference model, a softer symmetry energy was extracted. Two detailed reviews of the main experimental results concerning the isospin transport process and the comparisons with the prediction of the most high-performance models can be found in Refs. [36] and [37].

In such a scenario a setup like FAZIA (Refs. [38,39] and references therein), with extremely good capabilities in terms of isotopic identification (up to $Z = 25$ for ejectiles punching through the first 300-$\mu$m-thick silicon layer and up to $Z = 20$ for particles stopped in the first layer), can be very useful in shedding further light on the isospin transport phenomena and in better constraining the density dependence of the symmetry energy term; in fact, also in a reduced configuration, as the one used for the experiment described in this work, FAZIA is able to add new experimental data on this topic to the large amount of already published measurements. In this paper we report the experimental results concerning the isospin transport for the systems $^{80}$Kr + $^{40,48}$Ca at 35 MeV/nucleon using experimental data collected with a reduced setup (four blocks) during the first FAZIA experiment; this data set is the same analyzed in Ref. [40]. The event selection criteria have been checked by means of a transport model (antisymmetrized molecular dynamics AMD [41–43]) coupled with the statistical code GEMINI [26,28,44] as an afterburner, which was able to well reproduce the main features of the experimental events, as shown in Fig. 1 of Ref. [40]. From the comparison of the experimental results with the prediction of this model, some hints toward a stiff symmetry energy have been found (see Sec. IV C).

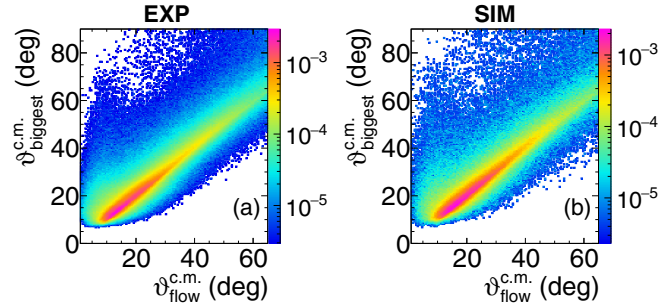


FIG. 1. Center-of-mass polar angle of the biggest fragment of the event $\vartheta^{c.m.}_{biggest}$ vs. flow angle $\vartheta^{c.m.}_{flow}$ for events with multiplicity $\geqslant 2$ for the system $^{80}$Kr + $^{48}$Ca. (a) Experimental data. (b) Simulated data (AMD + GEMINI++) filtered with a software replica of the setup.

## II. THE EXPERIMENT

As described in Ref. [40], the experiment took place at INFN-LNS, with a beam of $^{80}$Kr at 35 MeV/nucleon, delivered by the Ciclotrone Superconduttore (CS) cyclotron with an average current of 0.1 pnA, impinging on either of two 500-$\mu$g cm$^{-2}$-thick Ca targets, a neutron-deficient $^{40}$Ca and a neutron-rich $^{48}$Ca. Both targets were sandwiched between two thin (10-$\mu$g cm$^{-2}$-thick) layers of $^{12}$C to avoid prompt oxidation. The choice of a beam with $N/Z = 1.22$, in between that of both calcium targets (1.0 and 1.4), was specifically adopted to investigate the isospin transport looking at the properties of the QP residue and its decay products after reacting with a more or less neutron-rich target. Unfortunately the quality of the data collected with the $^{40}$Ca target is worse because a parasitic beam of $^{40}$Ar at the same beam energy was delivered together with the $^{80}$Kr beam; this fact requires more stringent conditions for the selection of the QP residue coming from the $^{80}$Kr beam, for example a very high lower limit ($Z > 18$) on the size of the QP residue when the $^{40}$Ca case is analyzed, thus rejecting the most dissipative events. The choice of $Z = 19$ as a lower limit for the QP residue is sufficient to exclude the pollution due to the $^{40}$Ar ($Z = 18$) parasitic beam; in fact, as it will be shown in Sec. III, in the analyzed data sample we want to exclude (via a proper cut, as shown in Fig. 2) central collisions, mostly producing a big source after incomplete fusion process. As a consequence, keeping only events in which the forward emitted (in center of mass) biggest fragment (i.e.,

[1]The symmetry energy is commonly expanded aroung $\rho_0$ as $E_{sym}(\rho) = S_0 + L\frac{(\rho-\rho_0)}{3\rho_0} + O[\frac{(\rho-\rho_0)^2}{9\rho_0^2}]$ [23]; the models for the symmetry energy are defined as stiff or soft depending on the value of the slope parameter $L$.

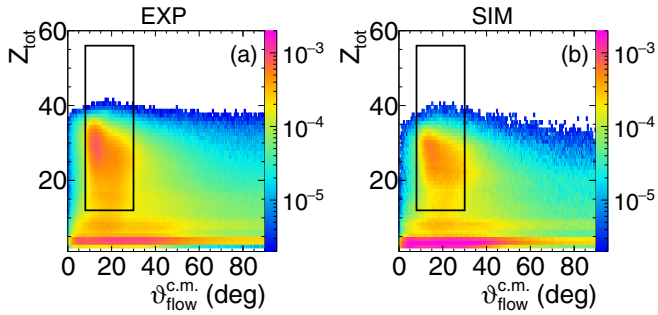


FIG. 2. $Z_{tot}$ vs. $\vartheta^{c.m.}_{flow}$ for events with multiplicity $\geqslant 2$ for the system $^{80}Kr + ^{48}Ca$. (a) Experimental data. (b) Simulated data (AMD + GEMINI++) filtered with a software replica of the setup. The black rectangle corresponds to the adopted selection for peripheral collisions.

the QP residue) has a charge greater than 18 very efficiently excludes from further analysis the spurious events originated by Ar-induced collisions. Only DIC events coming from the heavier Kr bream can fulfill the applied condition. Of course, we are aware that this cut excludes also the most dissipative collisions induced by the good Kr beam, where relatively light QP residues, with $Z \leqslant 18$, can be found at the end of the deexcitation chain.

The experimental setup, described in Ref. [40], consisted of four FAZIA blocks [38], for a total of 64 three-layer telescopes [300 $\mu$m Si–500 $\mu$m Si–10 cm CsI(Tl) read out by a photodiode], fully equipped with digital electronics, arranged in a belt configuration, covering the polar angles between 2.4° and 17.4°; a sketch of the setup can be found in Fig. 1 of Ref. [40] and in Fig. 1 of Ref. [45]. The isotopic identification was achieved up to $Z = 25$ for ions punching through the first Si layer and up to $Z = 20$ for particles stopped in it thanks to the pulse shape analysis. Since the grazing angle is around 2° for both investigated reactions, the geometrical configuration adopted in this experiment allowed to measure both the QP residue and the QP fission fragments, whose properties are the topic of Ref. [40].

## III. DATA ANALYSIS

Since this work is focused on the properties of the QP residue and of the midvelocity emission in semiperipheral events, binary events must be selected, after rejecting events with experimental multiplicity less than 2. Such a selection is obtained from the correlation between the total detected charge $Z_{tot}$ and the center-of-mass flow angle $\vartheta^{c.m.}_{flow}$ [46] built including all the ejectiles. Such an angle is defined starting from the momentum tensor $Q_{ij} = \sum_{n=1}^{N} \frac{p_i^{(n)} p_j^{(n)}}{p^{(n)}}$, where $p^{(n)}_{i(j)}$ is the $i(j)$ Cartesian component of the momentum $\vec{p}^{\,(n)}$ of the $n$th particle in the center-of-mass frame; the sum runs over all the detected products. Once the tensor is diagonalized, three eigenvalues $\lambda_i$, with $i = 1,2,3$, and three eigenvectors $\vec{e}_i$, with $i = 1,2,3$, are obtained. If $\lambda_1$ is the largest eigenvalue, then the flow angle is defined as the angle between the corresponding eigenvector $\vec{e}_1$ and the beam axis versor $\hat{u}_3$: $\cos(\vartheta^{c.m.}_{flow}) = |\vec{e}_1 \cdot \hat{u}_3|$. Due to the limited angular coverage of the setup, the flow angle is strictly correlated to the polar angle of the biggest fragment of the event, as shown in Fig. 1.

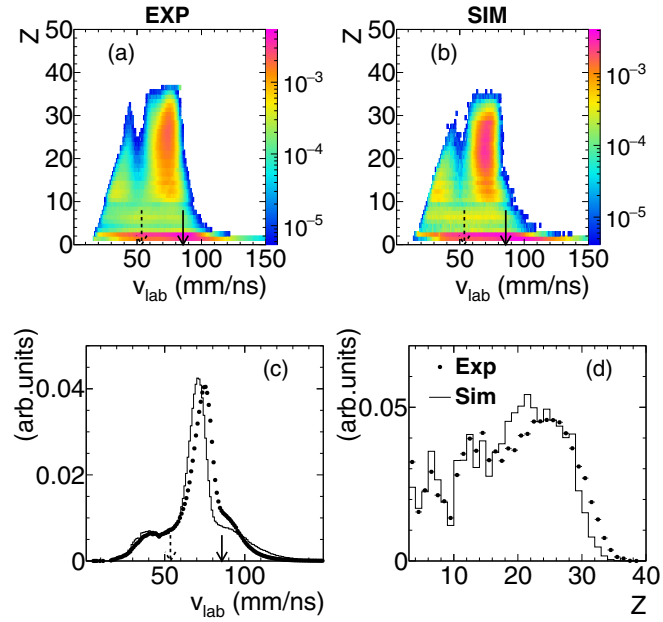


FIG. 3. Top: $Z$ vs. $v_{lab}$ for all the ejectiles of events fulfilling the semiperipheral selection for the reaction $^{80}Kr + ^{48}Ca$. (a) Experimental data. (b) AMD + GEMINI++. Bottom: (c) $v_{lab}$ distribution for experimental (symbols) and simulated (histograms) data. (d) $Z$ distribution for experimental (symbols) and simulated (histograms) data. The solid arrow corresponds to the beam velocity, while the dashed arrow corresponds to the center-of-mass velocity.

The adopted selection requires $8° \leqslant \vartheta^{c.m.}_{flow} \leqslant 30°$ and $Z_{tot} \geqslant 12$, as shown by the black rectangle in Fig. 2(a).

In order to check the validity of the adopted selection to identify semiperipheral binary events, the same condition was applied to simulated data produced by the AMD model [41–43] coupled to GEMINI [26,28,44] as an afterburner. The simulated data, filtered via a software replica of the setup, which takes into account both the geometrical coverage and the identification thresholds, were found to reproduce reasonably well the experimental data [40], as shown also in Fig. 2(b). Details about the version of the model used in this work (which includes cluster correlations) can be found in Refs. [40,47]. Here we only recall that AMD was run with both a stiff ($L = 108$ MeV) and a soft ($L = 46$ MeV) parametrization of the symmetry energy term (both of them with $S_0 = 32$ MeV) and that GEMINI was used both in its C++ version [28] and in the Fortran90 one [26,44], because some differences in the composition of the secondary deexcitation were observed depending on the used afterburner [47]. Unless otherwise mentioned, the stiff version of AMD (coupled to GEMINI++) is used.

The $Z$ vs. $v_{lab}$ correlation (where $v_{lab}$ is the laboratory velocity) for all the detected products in semiperipheral events (i.e., events falling inside the black rectangle of Fig. 2) is shown in the panels of Fig. 3 both for the experiment [Fig. 3(a)] and for the simulation [Fig. 3(b)], while in Fig. 3(c) and Fig. 3(d) the laboratory velocity and the charge

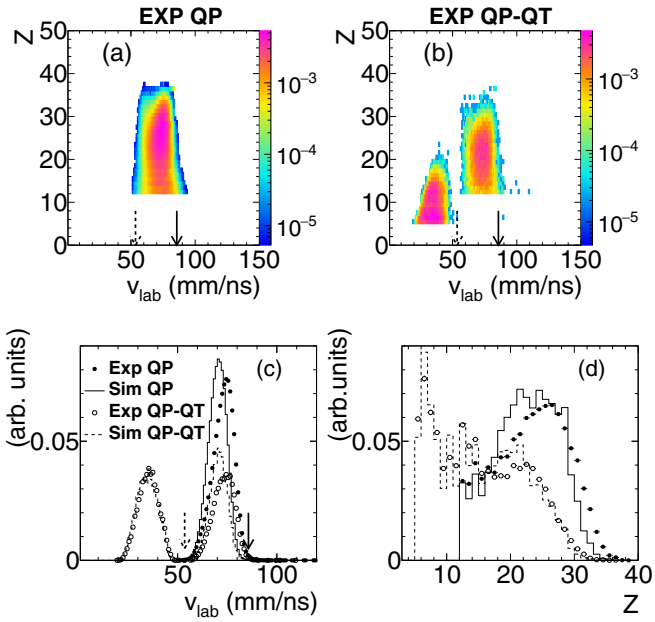


FIG. 4. Top: Experimental data for the system $^{80}$Kr + $^{48}$Ca. (a) $Z$ vs. $v_{lab}$ for the biggest fragment in events where only the QP residue is detected. (b) $Z$ vs. $v_{lab}$ for the biggest and the second biggest fragment in events where both QP and QT residues are detected. Bottom: (c) The $v_{lab}$ distribution for the plot (a) (solid circles) and (b) (open circles). (d) The $Z$ distribution for the plot (a) (solid circles) and (b) (open circles). Solid and dashed histograms are the corresponding simulated (AMD + GEMINI++) events. The solid arrow corresponds to the beam velocity, while the dashed arrow corresponds to the center-of-mass velocity.

distribution are shown, respectively. In this figure, both for the experimental [Fig. 3(a)] and the simulated case [Fig. 3(b)] the QP residue of binary reactions is clearly evident at velocity slightly smaller than the beam one (indicated by the solid arrow). In a minority of events also the QT residue is detected. The simulation reproduces reasonably well the experimental data, although there is a small shift in the QP residue velocity, with the experimental case less dissipative than the simulated one.

The events we are focusing on in this work are as follows: (i) events where only the QP residue, possibly accompanied by LCP and light IMF ($Z = 3$ and 4), is detected and (ii) events where both QP and QT residues are identified. In type (i) only one big fragment (with $Z \geqslant 12$ or $Z > 18$, with the latter condition used when $^{80}$Kr + $^{40}$Ca is considered, too) forward emitted in the center-of-mass frame is detected. In type (ii) two fragments are identified, one fulfilling the same conditions of the QP residue of type (i) and one with $Z \geqslant 5$; the relative angle in the center-of-mass frame between the two detected fragments must be $\vartheta_{rel}^{c.m.} \geqslant 160^{\circ}$. Here except for the discussion addressed in Sec. IV C, we reject the QP break up channel (events with two fragments and $40^{\circ} \leqslant \vartheta_{rel}^{c.m.} \leqslant 100^{\circ}$), which was the main subject of Ref. [40].

The $Z$ vs. $v_{lab}$ correlation for the biggest fragment for events in which only the QP residue is detected [type (i)] is shown in Fig. 4(a); the same plot for the biggest and the second biggest fragment of the event when QP and QT residues are detected [type (ii)] is shown in (b). The velocity distributions of the QP residue in both classes of events are very similar, as shown by solid circles and open circles in (c); the same behavior is observed also for simulated data [solid and dashed histograms in Fig. 4(c)], although the simulated events appear to be more dissipative. The charge of the QP residue when measured in coincidence with the QT residue [open points in Fig. 4(d)] is lower than when only a QP residue is detected (solid points). This observation, that the model nicely reproduces (as shown by solid and dashed lines), is related to the fact that type (ii) events are more dissipative. Indeed, due to the small angular coverage of the setup, in order to detect also the QT [type (ii)], the event must be more dissipative than in case of detection of the QP residue only [type (i)] and the charge of the QP residue is relatively well anticorrelated to the centrality of the reaction. In contrast, the QP residue velocity weakly depends on the centrality, thus explaining the similarity of the velocity distributions in type (i) and type (ii) events. The model supports this evidence as shown in Fig. 5, where the impact parameter distribution for the two classes of events is drawn. Although the distribution is rather broad in both cases, the average impact parameter for type (ii) events is 5.3 fm while it is 6.0 fm for type (i) events.

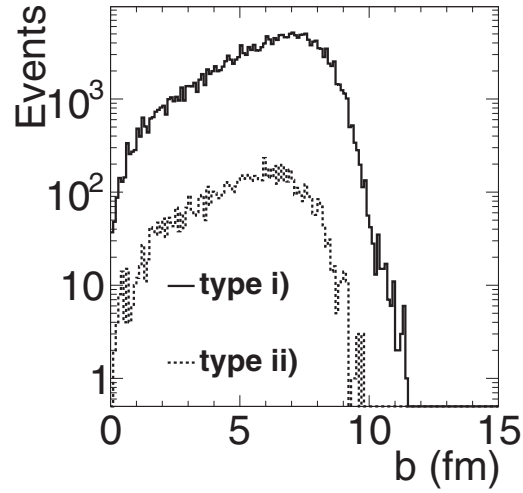


FIG. 5. Impact parameter distribution of type (i) (continuous line) and type (ii) (dashed line) events for the reaction $^{80}$Kr + $^{48}$Ca. Filtered simulated data (AMD + GEMINI++).

Concerning the contribution of the $^{12}$C background, the estimate made by means of a HIPSE simulation [48], as explained in Ref. [40], suggests that such contribution is absolutely negligible for events where also the QT is detected, while it reaches up to 1% when the QP residue only is measured. As a consequence, we can safely neglect the effect of the reactions on $^{12}$C in the analysis of these data.

## IV. RESULTS

### A. Isospin diffusion: Isotopic composition of the QP residue and its ejectiles

The most direct evidence of isospin diffusion can be obtained by comparing the isotopic composition of the QP

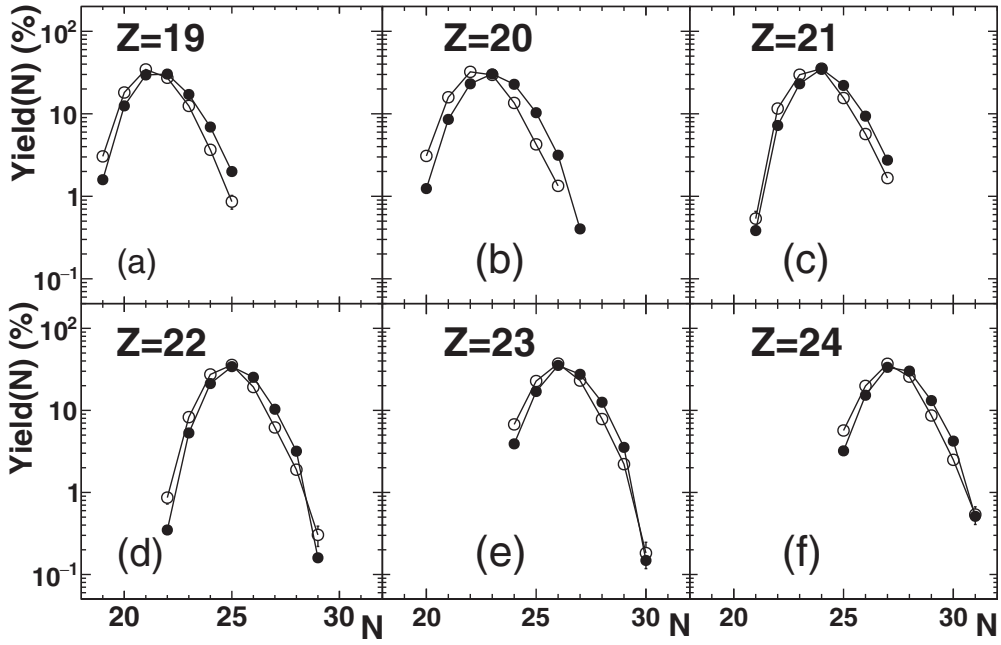


FIG. 6. Experimental isotopic distribution of the QP residue in the charge range $Z = 19$–$24$. Type (i) and type (ii) events are summed. Solid symbols: $^{80}$Kr + $^{48}$Ca. Open symbols: $^{80}$Kr + $^{40}$Ca.

residue when the target changes from $^{40}$Ca to $^{48}$Ca; of course this is possible only when the fragments are identified also in mass. The very good performance of FAZIA makes it possible to investigate the isotopic composition of the QP residue up to $Z = 25$, which, in any case, corresponds to rather dissipative reactions, being the charge of the projectile 36. However, we want to stress that the possibility to study the isospin diffusion process by looking at the isotopic composition of the QP residue in such a wide charge range and at the same time at its evaporated products is a peculiar strength of FAZIA, which makes its results competitive with those obtained by means of spectrometers. The obtained results are presented in Fig. 6, as open symbols for $^{80}$Kr + $^{40}$Ca and solid symbols for $^{80}$Kr + $^{48}$Ca, including both type (i) and type (ii) events without distinguishing; we have verified that in both systems the $\langle N\rangle/Z$ of the QP residue in type (ii) events is systematically slightly lower (by about 0.3%) than that of type (i) events. From this plot it clearly emerges that when the target is $^{48}$Ca the yield of the neutron-rich side is more populated with respect to the case of $^{40}$Ca. This indicates that in the investigated charge region (between 19 and 25) the $\langle N\rangle/Z$ of the QP residue for the $^{80}$Kr + $^{48}$Ca reaction is systematically higher by about 0.02 (i.e., less than 0.5 neutrons) than for $^{80}$Kr + $^{40}$Ca. This gives a direct evidence of isospin diffusion, as shown in the literature either on data collected with a spectrometer [10] (in this case covering all the QP residue charge range) or for a much lighter projectile [13].

The isotopic composition of particles forward emitted with respect to the QP residue (and hence mainly evaporated by the QP) is shown in Fig. 7 for both systems; their $\langle N\rangle/Z$ as a function of their charge is shown in Fig. 8, again for both reactions. The yield of protons largely dominates the $Z = 1$ emission [Fig. 7(a)], thus strongly reducing the $\langle N\rangle/Z$ for $Z = 1$ observed in Fig. 8. From such a figure we can see that when the target is $^{48}$Ca the emitted particles are slightly more neutron rich, with the possible exception of $Z = 2$; in that case the contribution of $\alpha$ particles is so dominant for

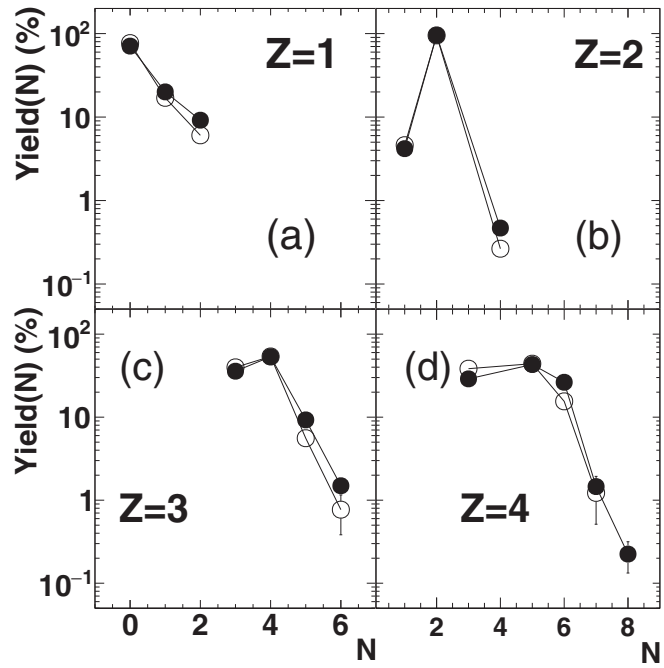


FIG. 7. Experimental isotopic distributions of particles forward emitted with respect to the QP residue in the charge range $Z =$ 1–4. Type (i) and type (ii) events are summed. Solid symbols: $^{80}$Kr + $^{48}$Ca. Open symbols: $^{80}$Kr + $^{40}$Ca.

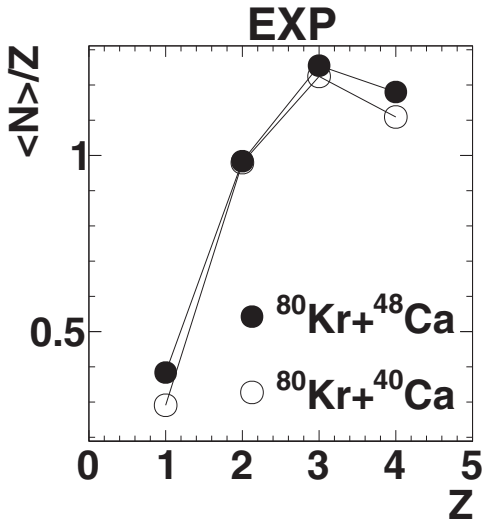


FIG. 8. Experimental $\langle N\rangle/Z$ vs. $Z$ for particles forward emitted with respect to the QP residue. Solid symbols: $^{80}\mathrm{Kr}+{}^{48}\mathrm{Ca}$. Open symbols: $^{80}\mathrm{Kr}+{}^{40}\mathrm{Ca}$

both reactions [as shown in Fig. 7(b)] that the effect of other isotopes is negligible ($\langle N\rangle/Z$ almost equal to 1 in both cases).

In any case, if we look at the yield ratio between $^{6}$He and $\alpha$ particles, as shown in Fig. 9, then we can see that the yield of the neutron-rich He isotope tends to increase with respect to the $\alpha$ when the target is the neutron-rich $^{48}$Ca, as expected. The same trend is observed for all isotopic and isobaric ratios shown in the plot: When the target is the neutron-rich one, the yield ratios (always calculated with the yields of the neutron-rich particles in the numerator) are higher, thus indicating that not only the isotopic composition of the QP residue (slightly) depends on the isospin of the target but also that of its evaporated particles, as shown for example also in Refs. [9,13,49].[2] In particular, it is possible to calculate the $N/Z$ event-averaged ratio for complex particles, which was introduced in Ref. [9] as $(\langle N\rangle/\langle Z\rangle)_{\mathrm{CP}} = \sum_{N_{\mathrm{ev}}}\sum_i N_i/\sum_{N_{\mathrm{ev}}}\sum_i Z_i$, where $N_{\mathrm{ev}}$ is the number of events, $N_i$ is the neutron number, and $Z_i$ is the proton number of forward emitted (with respect to the QP residue) ejectiles with $Z_i = 1$–4, but excluding free protons (the inclusion of free protons would require to include also free neutrons, which are undetected). The obtained results are $1.030 \pm 0.012$ for $^{80}\mathrm{Kr}+{}^{40}\mathrm{Ca}$ and $1.051 \pm 0.003$ for $^{80}\mathrm{Kr}+{}^{48}\mathrm{Ca}$, again demonstrating a neutron enrichment in the light ejectiles evaporated from the QP when the target is neutron rich.

### B. Isospin drift: Isotopic composition of light products as a function of their velocity

The limited angular coverage of the setup prevented us from separating in a clean way the midvelocity from the evaporative emission. However, it is reasonable to assume, as done in Sec. IV A, that the ejectiles forward emitted with respect to the QP residue are mainly the result of the evaporative decay of the QP. On the other hand, particles forward emitted with respect to the center-of-mass system, but backward with respect to the QP residue, are of multiple origin, because they include both the evaporation from the QP and the mid-velocity emission, although a contribution also from the QT cannot be categorically excluded. This last contribution may be present mainly when the relative velocity between QP and QT is small (in very dissipative collisions) and the Coulomb ridges of the emissions from the two reaction partners tend to partially overlap. In any case, as we will see, the results obtained for the reaction with the $^{40}$Ca target suggest that the target contribution is not so critical. In fact, in Fig. 10 some isobaric and isotopic yield ratios (with the neutron-rich ejectile always in the numerator) are shown, both for particles forward emitted with respect to the QP residue (circles), from now on called *forward* particles, and for particles forward emitted in the center of mass and backward emitted with respect to the QP residue (squares), from now on called *backward* particles.[3] It is evident that the ratios for backward particles are systematically higher than the ratios obtained for forward particles, i.e., there is a neutron enrichment in the backward emission. We observe that this enrichment is seen not only in Fig. 10(a), where an evaporative contribution from the neutron-rich target $^{48}$Ca might spuriously increase the isotopic composition of the backward emission with respect to the forward QP evaporation, but also in Fig. 10(b), where the target is less neutron-rich than the $^{80}$Kr projectile. Therefore these results suggest a neutron enrichment of the midvelocity emission, possibly related to the isospin drift mechanism. The same effect is seen in the $\langle N\rangle/Z$ vs. $Z$ of backward particles (not shown), which is systematically higher with respect to that of forward particles (shown in Fig. 8) for both systems, with a minimum difference for $Z = 2$ due to the fact that $\alpha$ particles always dominate the helium emission. The difference between the $\langle N\rangle/Z$ of backward and forward particles

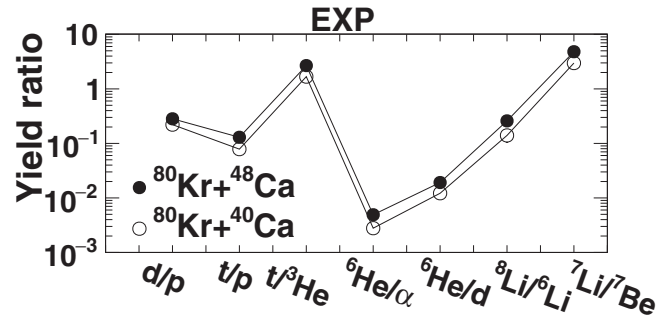


FIG. 9. Experimental yield ratio for particles forward emitted with respect to the QP residue. Solid symbols: $^{80}\mathrm{Kr}+{}^{48}\mathrm{Ca}$. Open symbols: $^{80}\mathrm{Kr}+{}^{40}\mathrm{Ca}$.

[2]The fact that the difference in $\langle N\rangle/Z$ for the QP residue when the target is changed from $^{40}$Ca to $^{48}$Ca is small may be partially due to the different secondary evaporation, more neutron rich for the $^{48}$Ca case and more neutron deficient for the $^{40}$Ca one.

[3]While the open circles of Fig. 10(b) are exactly the same as those of Fig. 9, the solid circles of Fig. 10(a) have been obtained reducing the minimum charge for the QP residue identification to $Z \geqslant 12$.

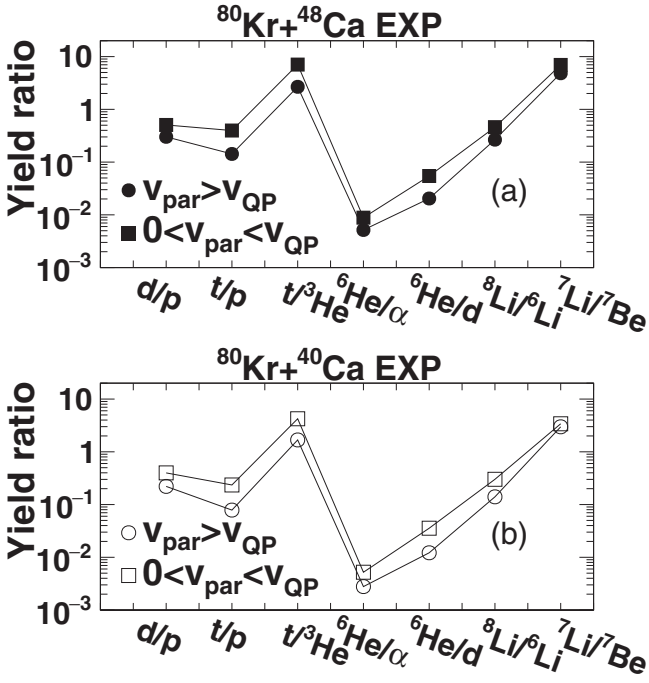


FIG. 10. Experimental yield ratio for forward (circles) and backward (squares) particles. Solid symbols: $^{80}\mathrm{Kr} + {}^{48}\mathrm{Ca}$ (minimum charge of the QP residue: 12). Open symbols: $^{80}\mathrm{Kr} + {}^{40}\mathrm{Ca}$ (minimum charge of the QP residue: 18).

is shown in Fig. 11 as a function of their $Z$ for both reactions, as in Fig. 7(c) of Ref. [12]. The difference is always positive, with a minimum for $Z = 2$ and a maximum for $Z = 1$; the effect is similar in both systems, as expected, because in this presentation the contribution of the isospin diffusion cancels out, since it affects in a similar way the evaporation from the QP in both forward and backward direction,[4] leaving only the outcome which may be ascribed to the isospin drift process, very similar for both reactions.

[4]A similar consideration can be applied also to the isospin fractionation, which takes place everywhere; as a consequence it is removed by the adopted subtraction procedure.

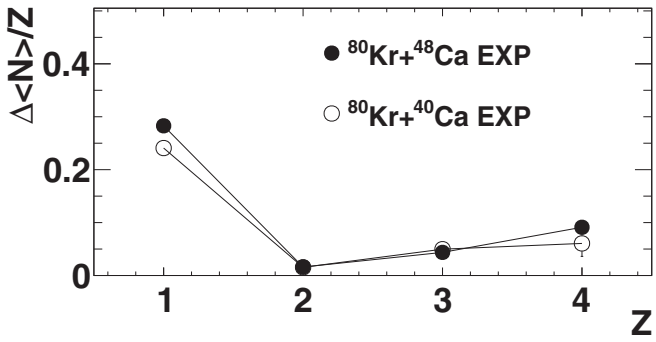


FIG. 11. Experimental difference between $\langle N\rangle/Z$ of backward and forward particles as a function of their $Z$ (minimum charge of QP residue: 18). Solid symbols: $^{80}\mathrm{Kr} + {}^{48}\mathrm{Ca}$. Open symbols: $^{80}\mathrm{Kr} + {}^{40}\mathrm{Ca}$.

### C. Hints toward a stiff symmetry energy

In the previous Secs. IV A and IV B we have put into evidence the presence, in the experimental data, of effects that can be attributed to the isospin diffusion and drift. In this section we will investigate the possibility to gain some hints on the stiffness of the symmetry energy from the comparison of the experimental results with the prediction of AMD plus GEMINI++, in particular looking at isospin drift related effects. In fact such effects should present a significant sensitivity to the stiffness of the symmetry energy, because they take place when a density gradient is established, i.e., when a part of the system moves away from $\rho_0$, and, in the hydrodynamical approximation of Ref. [19], the amount of the drift should depend on the density derivative of the symmetry energy.

A good sensitivity can be expected looking at the midvelocity emission, as it was done for example in Ref. [11], because the neck region is supposed to be more diluted than the QP/QT. We therefore first compare the isotopic distribution of midvelocity fragments with the prediction of AMD plus GEMINI++, running the dynamical code with different hypotheses on the stiffness of the symmetry energy.

The first and the second moment of the isotopic distribution, both of them as a function of $Z$, have been produced for ejectiles in the charge range $2 \leqslant Z \leqslant 11$ belonging to the backward selection of Sec. IV B. Such selection should include the maximum amount of midvelocity products, although it is not able to exclude evaporated particles emitted backward from the QP. In this sample also the lighter fragments of events classified as QP breakup (i.e., $40^\circ \leqslant \vartheta_{\mathrm{rel}}^{\mathrm{c.m.}} \leqslant 100^\circ$, see Ref. [40]) have been included, because there is no sharp boundary between the midvelocity emission and the asymmetric QP breakup with the light fragment backward emitted with respect to the QP. Hydrogen isotopes have been excluded because in AMD with the soft parametrization, corresponding to the SLy4 force in Ref. [50], the deuteron binding energy is largely overestimated and this fact produces an anomalous increase of their multiplicity [47].

The obtained results are plotted in Fig. 12 for the system $^{80}\mathrm{Kr} + {}^{48}\mathrm{Ca}$, where in Fig. 12(a) the $\langle N\rangle/Z$ vs. $Z$ and in Fig. 12(b) the second moment $\sigma_N$ of the isotopic distribution are shown. Solid circles correspond to the experimental data, while red (green) crosses are the simulation results with the stiff (soft) parametrization for the symmetry energy and using GEMINI++ as an afterburner.

The experimental $\langle N\rangle/Z$ vs. $Z$ [Fig. 12(a)] displays the typical features already observed in many works (for example, Fig. 7 of Ref. [12] and references therein): Starting from $Z = 3$ the average isospin first decreases when the charge $Z$ increases, with the exception of $Z = 7$ and $Z = 9$, and then flattens; the $\langle N\rangle/Z$ of $Z = 2$ is very close to 1 because $\alpha$ particles dominate. Concerning the simulated data, the most striking observation is that the experimental results are very well reproduced by the simulation; in particular, the $\langle N\rangle/Z$ of light fragments ($Z = 3$–5) is better reproduced by

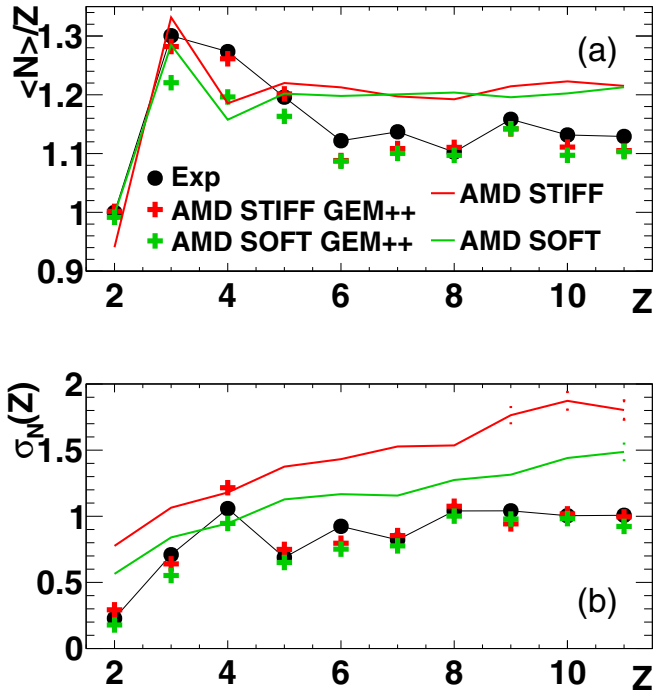


FIG. 12. (a) $\langle N\rangle/Z$ vs. $Z$ for light ejectiles backward emitted with respect to the QP residue and forward emitted with respect to the center of mass (b) Second moment of the isotopic distribution for the same ejectiles. Data refer to $^{80}$Kr + $^{48}$Ca. Black solid circles: Experimental data. Red crosses: AMD with stiff parametrization for the symmetry energy followed by GEMINI++ as an afterburner. Green crosses: AMD with soft parametrization for the symmetry energy followed by GEMINI++ as an afterburner. In addition to type (i) and type (ii) events, also QP fission events, considering the smaller fragment of the fission pair, have been included. Lines: AMD primary data (red: stiff, green: soft).

the stiff parametrization, while no sensitivity to the symmetry energy formula is obtained for higher $Z$ ejectiles (both parametrizations work well for these heavier products). The simulated data shown in the figure have been obtained using GEMINI++ as afterburner, but all these observations remain true also if GEMINI Fortran90 afterburner is used.

If we look at Fig. 12(b) for $\sigma_N$, first, we observe that the model really does a good job in reproducing the experimental data; unfortunately, this picture shows that the second moment of the isotopic distribution of the IMF is not able to give significant constraints on the symmetry energy. In fact the experimental behavior, which displays a staggering trend, with broader mass distributions for even $Z$ (with the exception of $Z = 2$, where $\alpha$ emission is dominant) is reasonably well reproduced by both parametrizations with GEMINI++ afterburner, with no clear indications in favor of one of them. When GEMINI Fortran90 is used (not shown), the second moment is systematically slightly overestimated, except for $Z = 3$ and $Z = 6$ (where data are well reproduced), but again no clear indication concerning the stiffness of the symmetry energy is obtained.

As stated in the Introduction, in the present AMD calculation the first-order coefficient for the expansion of the symmetry energy as a function of the density changes from $L = 108$ MeV for the stiff parametrization to $L = 46$ MeV for the soft one. In view of such a variation the largest observed changes in the $\langle N\rangle/Z$ shown in Fig. 12(a) are of the order of 0.1 at the level of secondary fragments. Since, as shown in Fig. 11, the effect of the isospin drift itself on $\langle N\rangle/Z$ is of the order of 0.1 for $Z = 4$, the fact that we observe variations of the same order on this observable when the symmetry energy recipe is changed from a stiff one (where the drift is enhanced) to a soft one (where the drift mechanism is damped) is fully understandable and within the expectations.

Until now we have discussed the postevaporation results of the simulation; if we look at primary data (lines in Fig. 12) we can see that there is a significant difference between the stiff and the soft parametrizations for $\sigma_N$ [Fig. 12(b)], as suggested in Ref. [51]; in particular, for the stiff case, the isotopic distribution is wider. Concerning $\langle N\rangle/Z$ [Fig. 12(a)], for heavy IMF the difference between the two parametrizations is indeed negligible, while it reaches a maximum value of 6% for light $Z$.

A possible explanation of the negligible difference between the two symmetry energy parametrizations for the first moment of the isotopic distribution of the IMF at the level of primary fragments may arise from the fact that on the results presented in Fig. 12(a) there are conflicting contributions at work. In particular, we are looking at the cumulative effects of diffusion, drift, and fractionation, which produce contrasting or even opposite effects on the isotopic composition of the IMF and whose strength depends in different (also opposite) ways on the symmetry energy. For example, with the soft symmetry energy, the isospin drift is weaker, while the isospin diffusion is stronger and also the isospin fractionation, which tends to make the IMF more symmetric, is stronger.

For both parametrizations of the symmetry energy the application of the afterburner tends to reduce the width of the isotopic distribution and to decrease the $\langle N\rangle/Z$, except for very light IMF, which in addition are more affected by the side feeding process from heavier products. The final result of the decay process is that the second moment loses its sensitivity to the stiffness of the symmetry energy, while, concerning $\langle N\rangle/Z$, the difference between the stiff and the soft parametrization for $Z = 3$–5 becomes larger than that observed for primary fragments. In particular, for both primary and secondary data the Li and Be isotopes are more neutron rich when the symmetry energy is stiff compared with the case of the soft symmetry energy. For the secondary fragments, the difference is about 0.06 in $\langle N\rangle/Z$ (or about 0.2 in $\langle N\rangle$) for these light IMF. This may be interpreted as an effect of isospin drift which should be strong for the stiff symmetry energy. However, a qualitatively similar dependence on the symmetry energy is expected in principle from the isospin fractionation which allows more neutron-rich fragments when the symmetry energy is stiff.

An attempt at eliminating the fractionation effect can be done by looking at the difference between $\langle N\rangle$ of backward and forward particles as a function of their $Z$ (as in Fig. 11, but without dividing by $Z$ just to emphasize the result for heavier fragments), as shown in Fig. 13 again for the $^{48}$Ca target. In fact, the isospin fractionation is expected to be independent

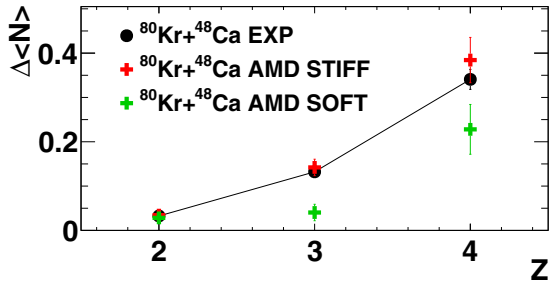


FIG. 13. Difference between $\langle N\rangle$ of backward and forward particles as a function of their $Z$ for the system $^{80}$Kr + $^{48}$Ca (minimum charge of QP residue: 12). Black circles: Experimental data; red crosses: Stiff AMD+GEMINI++; green crosses: Soft AMD+GEMINI++.

of the emission direction thus affecting in a similar way both forward and backward emissions; therefore it should cancel out in their difference. We find that the obtained symmetry energy dependence for $Z = 3$ and 4 is not much reduced with respect to that in Fig. 12(a), suggesting the existence of symmetry energy effects beyond isospin fractionation. Moreover the good agreement of the calculations with the experimental results seems to favor the stiff symmetry energy. Although the statistical uncertainty is large for these fragments after applying the geometrical filter corresponding to the experimental situation, a similar dependence is observed for the fragments also before applying the filter (e.g., the difference of $\Delta\langle N\rangle$ between the stiff and soft case without the experimental filter is 0.24 for $Z = 4$).

Concerning the $^{80}$Kr + $^{40}$Ca system, no indication about the stiffness of the symmetry energy can be derived comparing the experimental $\Delta\langle N\rangle$ with the simulated one. The lower collected statistics for this system and the more stringent condition on the QP selection because of the $^{40}$Ar pollution make it impossible to draw any clear conclusion from the inspection of the neutron content of $Z = 2$–4. A higher amount of statistics would be necessary to clarify the behavior of this system.

Concerning the isospin diffusion process, in the $^{80}$Kr + $^{48}$Ca system the target is more neutron rich than the projectile. Therefore, right after the diffusion has started, more protons than neutrons will flow out of the projectile, making the neck region less neutron rich and the backward side of the projectile more neutron rich. However, as the diffusion progresses, neutrons from the target move toward the projectile, thus neutron-enriching the neck. Then, if the diffusion ends before the total isospin equilibration, the backward side of the projectile (and the neck zone) may be more neutron rich than the forward side. Therefore, it is not evident how the isospin diffusion, which is known to be stronger when the symmetry energy is soft, affects the $\langle N\rangle/Z$ of the backward side of the projectile. It is then important to extend this study by varying the combination of projectile and target.

If we compare the total yields of the different isotopes predicted by the model for the two stiffnesses of the symmetry energy, without trying to disentangle the different contributions, as shown in Fig. 14, then we can put into evidence the isotopic regions in which we can expect to obtain a better sensitivity to the symmetry energy formula. In Fig. 14 the ratios between the yields of the different isotopes produced by the stiff and the soft simulations are shown, both for $4\pi$ data (i.e., without applying the geometrical filter) and for filtered ones. The maximum sensitivity to the stiffness of the symmetry energy occurs where the ratios are appreciably different from 1. This appears to be the case for the most neutron-rich isotopes, without substantial modifications due to the geometrical filter.

Therefore, as shown in Fig. 15, we normalized the yields of He, Li, and Be isotopes to those for which the ratio stiff/soft is close to 1, namely $^{4}$He for $Z = 2$, $^{7}$Li for $Z = 3$, and $^{9}$Be for $Z = 4$, in order to increase the sensitivity to the adopted parametrization of the symmetry energy.

Unfortunately, these data do not offer a clear answer concerning the best recipe for the symmetry energy; in any case, in all the cases in which the two parametrizations give different values, the stiff calculation is closer to the experimental data. In particular, in the soft case $^{9}$Li and $^{12}$Be are not observed in the selected simulated sample, namely the

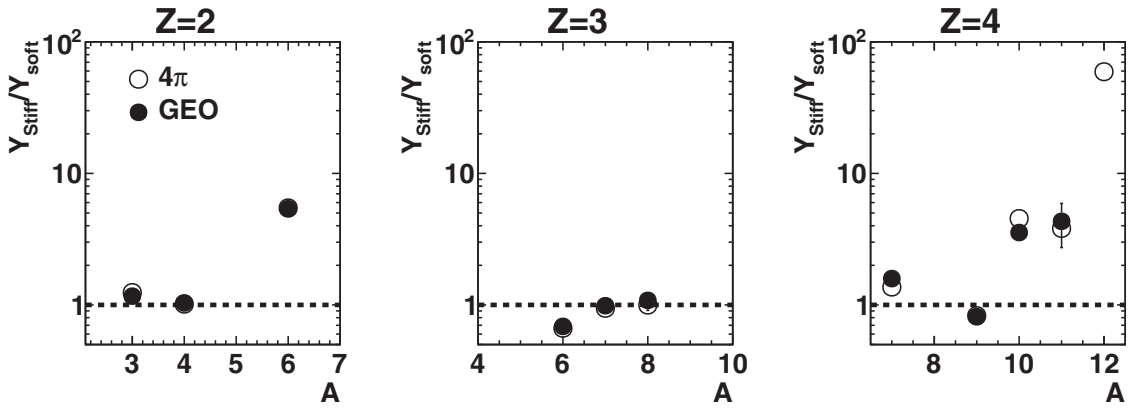


FIG. 14. AMD+GEMINI++: Ratios between the yields produced by the stiff and the soft calculations. All particles forward emitted in the center of mass are included.

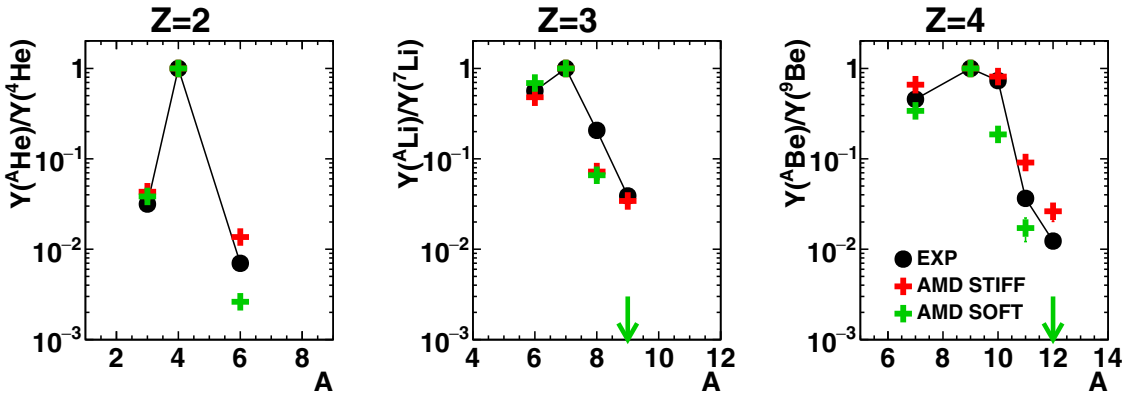


FIG. 15. AMD+GEMINI++ and experimental data: Yields of the different isotopes normalized to $^4$He for $Z = 2$, $^7$Li for $Z = 3$, and $^9$Be for $Z = 4$. All particles forward emitted in the center of mass are included. Green arrows are upper limits and indicate out-of-scale yield ratios.

ratio $^9$Li / $^7$Li ($^{12}$Be / $^9$Be) is smaller than $5 \times 10^{-4}$ ($1 \times 10^{-3}$). Therefore the dependence on the symmetry energy observed in $\sigma_N(Z)$ of the primary fragments may survive in the yield of neutron-rich fragments in the final state. To corroborate this statement, we have also verified that $^9$Li and $^{12}$Be are mainly directly produced in the dynamical stage.

The general conclusion of the presented analysis is that it is necessary to rely on other observables and other techniques to obtain more reliable constraints on the symmetry energy. An example could be the isospin transport ratio, as in the experimental program of INDRA-FAZIA at GANIL. Moreover, in order to better evidence the isospin drift effect, it is convenient to choose collisions between nuclei with the same $N/Z$ (but not with $N = Z$ because in the hydrodinamical picture of Ref. [19] the drift term disappears in symmetric matter), where the diffusion process is not present.

Another aspect worth noting is the fact that our results weakly point toward a value for the first-order term ($L = 108$ MeV) at the upper limit (or beyond) of recent compilations (see for example Fig. 3 of Ref. [33] or Fig. 1 of Ref. [52] or Ref [24]); anyhow, since the fragment yields can also depend on physical ingredients other than the symmetry energy parameter $L$, it is clear that the indicated value must not be considered as an absolute estimate, but it shows only a trend toward a stiff-kind behavior of the symmetry energy.

## V. SUMMARY AND CONCLUSIONS

This work deals with the analysis of experimental data, collected with four FAZIA blocks, for the systems $^{80}$Kr + $^{40,48}$Ca at 35 MeV/nucleon; these data were also the subject of Ref. [40], focused on the QP break up. In this paper experimental evidences of both kinds of isospin transport phenomena (drift and diffusion) in semiperipheral events have been shown. Concerning the isospin diffusion, the isotopic distribution of the QP residue (for $Z \leqslant 25$, where the isotopic resolution is experimentally available) obtained when the target was $^{40}$Ca was compared with that obtained with the neutron-rich target, finding a shift toward more neutron-rich isotopes when the target was $^{48}$Ca. A similar signal, both in the average isotopic composition and in the isobaric/isotopic ratios, was found also looking at the ejectiles evaporated by the QP.

The experimental data have been compared with the prediction of a simulation based on the AMD model, followed by GEMINI (both in the C++ and in the Fortran 90 version) as an afterburner, which already proved to be able to well reproduce this kind of reactions [40,47]; also in this case it gave very good results. The simulation was used both to check the validity of the applied conditions to select the desired channels and to find some possible constraint on the density dependence of the symmetry energy; for this latter purpose AMD was run with both a stiff and a soft parametrization. A weak hint toward a stiff symmetry energy, independently of the used afterburner, was found looking at the average isotopic composition of light products backward emitted with respect to the QP residue and forward emitted in the center of mass, i.e., in the region where the midvelocity contribution is significant. Anyhow, it is clear that the investigated observable is not able to give a stringent constraint on this dependence; more complete data, including isospin-symmetric and isospin-asymmetric systems in order to exploit the isospin transport ratio, are mandatory. In such scenario, the first INDRA-FAZIA campaign at GANIL should supply data of good quality and completeness, allowing more stringent constraints on the results of the theoretical models.

## ACKNOWLEDGMENTS

This work required the use of a lot of computation time for the production of the simulated data. We thank the GARR Consortium for the kind use of the cloud computing infrastructure on the platform cloud.garr.it. We thank also the INFN-CNAF for the use of its cloud computing infrastructure. A. Ono acknowledges support from Japan Society for the Promotion of Science KAKENHI Grant No. JP17K05432. This work was supported by the Polish National Science Centre under Contract No. 2014/14/M/ST2/00738 (COPIN-INFN Collaboration). The research leading to these results has received funding from the European Union HORIZON2020 reasearch and innovation programme under Grant Agreement No. 654002-ENSAR2. We acknowledge M. Bruno, who strongly contributed to the success of FAZIA.

[1] J. F. Dempsey, R. J. Charity, L. G. Sobotka, G. J. Kunde, S. Gaff, C. K. Gelbke, T. Glasmacher, M. J. Huang, R. C. Lemmon, W. G. Lynch *et al.*, Phys. Rev. C **54**, 1710 (1996).

[2] Y. Larochelle, L. Gingras, G. C. Ball, L. Beaulieu, P. Gagné, E. Hagberg, Z. Y. He, D. Horn, R. Laforest, R. Roy, and C. St-Pierre, Phys. Rev. C **62**, 051602(R) (2000).

[3] M. B. Tsang, T. X. Liu, L. Shi, P. Danielewicz, C. K. Gelbke, X. D. Liu, W. G. Lynch, W. P. Tan, G. Verde, A. Wagner, H. S. Xu, W. A. Friedman, L. Beaulieu, B. Davin, R. T. de Souza, Y. Larochelle, T. Lefort, R. Yanez, V. E. Viola, R. J. Charity, and L. G. Sobotka, Phys. Rev. Lett. **92**, 062701 (2004).

[4] D. Thériault, J. Gauthier, F. Grenier, F. Moisan, C. St-Pierre, R. Roy, B. Davin, S. Hudan, T. Paduszynski, R. T. deSouza *et al.*, Phys. Rev. C **74**, 051602(R) (2006).

[5] S. Piantelli, P. R. Maurenzig, A. Olmi, L. Bardelli, M. Bini, G. Casini, A. Mangiarotti, G. Pasquali, G. Poggi, and A. A. Stefanini, Phys. Rev. C **76**, 061601(R) (2007).

[6] T. X. Liu, W. G. Lynch, M. B. Tsang, X. D. Liu, R. Shomin, W. P. Tan, G. Verde, A. Wagner, H. F. Xi, H. S. Xu, B. Davin, Y. Larochelle, R. T. deSouza, R. J. Charity, and L. G. Sobotka, Phys. Rev. C **76**, 034603 (2007).

[7] I. Lombardo, C. Agodi, R. Alba, F. Amorini, A. Anzalone, I. Berceanu *et al.*, Phys. Rev. C **82**, 014608 (2010).

[8] A. L. Keksis, L. W. May, G. A. Souliotis, M. Veselsky, S. Galanopoulos, Z. Kohley, D. V. Shetty, S. N. Soisson, B. C. Stein, R. Tripathi, S. Wuenschel, S. J. Yennello, and B. A. Li, Phys. Rev. C **81**, 054602 (2010).

[9] E. Galichet, M. F. Rivet, B. Borderie, M. Colonna, R. Bougault, A. Chbihi *et al.* (INDRA Collaboration), Phys. Rev. C **79**, 064614 (2009).

[10] G. A. Souliotis, M. Veselsky, S. Galanopoulos, M. Jandel, Z. Kohley, L. W. May, D. V. Shetty, B. C. Stein, and S. J. Yennello, Phys. Rev. C **84**, 064607 (2011).

[11] E. De Filippo *et al.*, Phys. Rev. C **86**, 014610 (2012).

[12] S. Barlini, S. Piantelli, G. Casini, P. R. Maurenzig, A. Olmi, M. Bini *et al.* (FZIA Collaboration), Phys. Rev. C **87**, 054607 (2013).

[13] S. Piantelli, S. Valdré, S. Barlini, G. Casini, M. Colonna, G. Baiocco, M. Bini, M. Bruno, A. Camaiani, S. Carboni, M. Cicerchia, M. Cinausero, M. D'Agostino, M. Degerlier, D. Fabris, N. Gelli, F. Gramegna, D. Gruyer, V. L. Kravchuk, J. Mabiala, T. Marchi, L. Morelli, A. Olmi, P. Ottanelli, G. Pasquali, and G. Pastore, Phys. Rev. C **96**, 034622 (2017).

[14] L. W. May, A. Wakhle, A. B. McIntosh, Z. Kohley, S. Behling, A. Bonasera, G. Bonasera, P. Cammarata, K. Hagel, L. Heilborn, A. Jedele, A. Raphelt, A. R. Manso, G. Souliotis, R. Tripathi, M. D. Youngs, A. Zarrella, and S. J. Yennello, Phys. Rev. C **98**, 044602 (2018).

[15] R. Tribble *et al.*, Nucl. Instrum. Methods A **285**, 441 (1989).

[16] P. Milazzo, G. Vannini, C. Agodi, R. Alba, G. Bellia, M. Bruno, M. Colonna, N. Colonna, R. Coniglione, M. D'Agostino, A. D. Zoppo, L. Fabbietti, P. Finocchiaro, F. Gramegna, I. Iori, K. Loukachine, C. Maiolino, G. Margagliotti, P. Mastinu, E. Migneco, A. Moroni, P. Piattelli, R. Rui, D. Santonocito, P. Sapienza, and M. Sisto, Nucl. Phys. A **703**, 466 (2002).

[17] F. Rami *et al.* (FOPI Collaboration), Phys. Rev. Lett. **84**, 1120 (2000).

[18] A. Camaiani *et al.*, Phys. Rev. C **102**, 044607 (2020).

[19] V. Baran, M. Colonna, M. DiToro, M. Zielinska-Pfabé, and H. H. Wolter, Phys. Rev. C **72**, 064620 (2005).

[20] H. Müller and B. D. Serot, Phys. Rev. C **52**, 2072 (1995).

[21] A. Ono, P. Danielewicz, W. A. Friedman, W. G. Lynch, and M. B. Tsang, Phys. Rev. C **68**, 051601(R) (2003).

[22] A. Ono, P. Danielewicz, W. A. Friedman, W. G. Lynch, and M. B. Tsang, Phys. Rev. C **70**, 041604(R) (2004).

[23] M. B. Tsang, J. R. Stone, F. Camera, P. Danielewicz, S. Gandolfi, K. Hebeler, C. J. Horowitz, J. Lee, W. G. Lynch, Z. Kohley, R. Lemmon, P. Möller, T. Murakami, S. Riordan, X. Roca-Maza, F. Sammarruca, A. W. Steiner, I. Vidaña, and S. J. Yennello, Phys. Rev. C **86**, 015803 (2012).

[24] J. Margueron, R. Hoffmann Casali, and F. Gulminelli, Phys. Rev. C **97**, 025805 (2018).

[25] M. Colonna *et al.*, Nucl. Phys. A **642**, 449 (1998).

[26] R. J. Charity *et al.*, Nucl. Phys. A **483**, 371 (1988).

[27] R. Charity, K. Jing, D. Bowman, M. McMahan, G. Wozniak, L. Moretto, N. Colonna, G. Guarino, A. Pantaleo, L. Fiore, A. Gobbi, and K. Hildenbrand, Nucl. Phys. A **511**, 59 (1990).

[28] R. J. Charity, Phys. Rev. C **82**, 014610 (2010).

[29] E. Galichet, M. Colonna, B. Borderie, and M. F. Rivet, Phys. Rev. C **79**, 064615 (2009).

[30] D. Durand, Nucl. Phys. A **541**, 266 (1992).

[31] P. Napolitani, M. Colonna, F. Gulminelli, E. Galichet, S. Piantelli, G. Verde, and E. Vient, Phys. Rev. C **81**, 044619 (2010).

[32] G. Bertsch and S. D. Gupta, Phys. Rep. **160**, 189 (1988).

[33] M. B. Tsang, Y. Zhang, P. Danielewicz, M. Famiano, Z. Li, W. G. Lynch, and A. W. Steiner, Phys. Rev. Lett. **102**, 122701 (2009).

[34] Z. Y. Sun, M. B. Tsang, W. G. Lynch, G. Verde, F. Amorini, L. Andronenko, M. Andronenko, G. Cardella, M. Chatterje, P. Danielewicz, E. De Filippo, P. Dinh, E. Galichet, E. Geraci, H. Hua, E. La Guidara, G. Lanzalone, H. Liu, F. Lu, S. Lukyanov, C. Maiolino, A. Pagano, S. Piantelli, M. Papa, S. Pirrone, G. Politi, F. Porto, F. Rizzo, P. Russotto, D. Santonocito, and Y. X. Zhang, Phys. Rev. C **82**, 051603(R) (2010).

[35] Y. Zhang, P. Danielewicz, M. Famiano, Z. Li, W. Lynch, and M. Tsang, Phys. Lett. B **664**, 145 (2008).

[36] M. Colonna, Prog. Part. Nucl. Phys. **113**, 103775 (2020).

[37] A. B. McIntosh and S. J. Yennello, Prog. Part. Nucl. Phys. **108**, 103707 (2019).

[38] R. Bougault, G. Poggi, S. Barlini, B. Borderie, G. Casini, A. Chbihi, N. Le Neindre, M. Parlog, G. Pasquali, S. Piantelli *et al.*, Eur. Phys. J. A **50**, 47 (2014).

[39] S. Valdré *et al.*, Nucl. Instrum. Methods A **930**, 27 (2019).

[40] S. Piantelli, G. Casini, A. Ono, G. Poggi, G. Pastore, S. Barlini, A. Boiano, E. Bonnet, B. Borderie, R. Bougault, M. Bruno, A. Buccola, A. Camaiani, A. Chbihi, M. Cicerchia, M. Cinausero, M. D'Agostino, M. Degerlier, J. A. Dueñas, Q. Fable, D. Fabris, J. D. Frankland, C. Frosin, F. Gramegna, D. Gruyer, M. Henri, A. Kordyasz, T. Kozik, N. Le Neindre, I. Lombardo, O. Lopez, G. Mantovani, T. Marchi, L. Morelli, A. Olmi, P. Ottanelli, M. Pârlog, G. Pasquali, A. A. Stefanini, G. Tortone, S. Upadhyaya, S. Valdré, G. Verde, E. Vient, M. Vigilante, R. Alba, and C. Maiolino, Phys. Rev. C **101**, 034613 (2020).

[41] A. Ono, H. Horiuchi, T. Maruyama, and A. Ohnishi, Phys. Rev. Lett. **68**, 2898 (1992).

[42] A. Ono, Phys. Rev. C **59**, 853 (1999).

[43] A. Ono, J. Phys.: Conf. Ser. **420**, 012103 (2013).

[44] R. J. Charity, Phys. Rev. C **58**, 1073 (1998).

[45] G. Pastore, D. Gruyer, P. Ottanelli, N. L. Neindre, G. Pasquali, R. Alba, S. Barlini, M. Bini, E. Bonnet, B. Borderie *et al.*, Nucl. Instrum. Methods A **860**, 42 (2017).

[46] J. Cugnon and D. L'hote, Nucl. Phys. A **397**, 519 (1983).
[47] S. Piantelli, A. Olmi, P. R. Maurenzig, A. Ono, M. Bini, G. Casini, G. Pasquali, A. Mangiarotti, G. Poggi, A. A. Stefanini, S. Barlini, A. Camaiani, C. Ciampi, C. Frosin, P. Ottanelli, and S. Valdré, Phys. Rev. C **99**, 064616 (2019).
[48] D. Lacroix, A. Van Lauwe, and D. Durand, Phys. Rev. C **69**, 054604 (2004).
[49] R. Bougault, E. Bonnet, B. Borderie, A. Chbihi, D. Dell'Aquila, Q. Fable, L. Francalanza, J. D. Frankland, E. Galichet, D. Gruyer, D. Guinet, M. Henri, M. La Commara, N. Le Neindre, I. Lombardo, O. Lopez, L. Manduci, P. Marini, M. Pârlog, R. Roy, P. Saint-Onge, G. Verde, E. Vient, and M. Vigilante (INDRA Collaboration), Phys. Rev. C **97**, 024612 (2018).
[50] E. Chabanat, P. Bonche, P. Haensel, J. Meyer, and R. Schaeffer, Nucl. Phys. A **635**, 231 (1998).
[51] A. R. Raduta and F. Gulminelli, Phys. Rev. C **75**, 044605 (2007).
[52] B.-A. Li and X. Han, Phys. Lett. B **727**, 276 (2013).